Monthly Notices
of the
ROYAL ASTRONOMICAL SOCIETY

MNRAS **449,** 1704–1715 (2015) doi:10.1093/mnras/stv316

Multicolour time series photometry of four short-period weak-lined T Tauri stars

C. Koen★

Department of Statistics, University of the Western Cape, Private Bag X17, Bellville, 7535 Cape, South Africa

Accepted 2015 February 11. Received 2015 February 11; in original form 2014 August 6

ABSTRACT

The paper describes continuous photometric monitoring of four pre-main-sequence stars, probable members of young stellar associations. Measurements, covering at least four nights per star, were obtained by cycling through several filters. The data could be used to choose between aliases of rotation periods quoted in the literature. As expected, the amplitudes of sinusoidal variations decline with increasing wavelength, mildly enough to indicate the presence of coolspots on the stellar surfaces. Variability amplitudes can dwindle from a 0.1 mag level to virtually zero on a time-scale of one or two days. A flare observed in CD-36 3202 is discussed in some detail, and a useful mathematical model for its shape is introduced. It is demonstrated that accurate colour indices ($\sigma < 5$–6 mmag, typically) can be derived from the photometry. The magnitude variations as measured through different filters are linearly related. This is exploited to calculate spot temperatures (800–1150 K below photospheric for the different stars) and the ranges of variation of the spot filling factors (roughly 10–20 per cent). The available All Sky Automated Survey measurements of the stars are analysed, and it is concluded that there is good evidence for differential rotation in all four stars.

Key words: stars: flare – stars: individual: CD-36 3202 – stars: individual: CD-49 1902 – stars: individual: CD-66 395 – stars: individual: CD-72 248 – stars: variables: T Tauri, Herbig Ae/Be.

1 INTRODUCTION

A very large number of studies of photometric variability of T Tauri stars have seen the light. Observing campaigns which stretched over several years, and hence provide information about long time-scale brightness changes in these young stars, have been described by Herbst et al. (1994) and Grankin et al. (2007, 2008). Recently, there has been particular interest in deducing rotation periods in the pre-main-sequence stage of evolution from periodic variability in T Tauris – see Herbst et al. (2007) for a review, with many references.

Continuous monitoring of these stars on time-scales of minutes or shorter has been rare. The author is aware of the following: Smith, Jones & Clarke (1996) obtained *UBV* photometry of four classical T Tauri stars (CTTSs), observing each for several hours, on more than one night. Fernández et al. (2004) reported on an intensive observing campaign on V410 Tau, during which multicolour observations were made of flares. Günther et al. (2010) searched for, but failed to find, periodic variability at the subsecond level in two CTTSs. Two multicolour photometric studies of the multiperiodic T Tauri star UNSW-V760 were presented by Koen (2011, 2012). Very impressive single-filter light curves of a few T Tauri stars, stretching over days, have been obtained by using telescopes in space – see Siwak et al. (2011) and Silva-Valio & Lanza (2011).

This work most closely resembles that of Smith et al. (1996), but the targets were weak lined T Tauri stars (WTTSs) rather than CTTSs. The aim here was also to obtain detailed information about the forms of short time-scale (minutes to hours) variability, and its dependence on wavelength. Each of the four targets, taken from Torres et al. (2006), was observed continuously for several hours, on at least four nights. Short-period systems were selected so that in most cases full cycles could be covered in one night of observing.

All four stars are bright ROSAT sources showing lithium absorption and very rapid rotation, and hence are presumably young. Photometry from the All Sky Automated Survey (ASAS) has given periodicities shorter than a day in all four cases (Kiraga 2012). Re-analysis by Messina et al. (2011) of the ASAS data, supplemented by data from the SUPERWASP project (Pollacco et al. 2006), confirmed that periods are short, albeit mostly with revised values. Pertinent information can be found in Table 1. Given the late spectral types and youth, but absence of significant Hα emission, the objects can be classed as weak-lined or post-T Tauri stars (e.g. Stahler & Palla 2004).

The four stars are probable members of three different associations – Octans (age ∼20 Myr), Columba (30 Myr) and Argus (40 Myr) (Da Silva et al. 2009). (Note though that later work by

★ E-mail: ckoen@uwc.ac.za

Table 1. Information about the target stars. Data in columns 4–8 are from Torres et al. (2006), and the association memberships in column 2 are from Da Silva et al. (2009). Periods in columns 9–11 are from ASAS (Kiraga 2012), Messina et al. (2011) and this paper, respectively. The *J* and *FUV* magnitudes were extracted from the Two Micron All Sky Survey (2MASS – Skrutskie et al. 2006) and *Galaxy Evolution Explorer* (*GALEX* – Bianchi et al. 2011) catalogues, using the VizieR query service of the Centre de Données Astronomiques de Strasbourg.

Name	Association	*FUV*	*V*	*J*	Spectrum	$v \sin i$ (km s^{-1})	Li (mÅ)	P_1 (d)	P_2 (d)	P_3 (d)
CD-36 3202	Columba	20.73	11.22	9.41	K2Ve	170 (17)	300	0.235 33	0.307	0.235
CD-49 1902	Argus		11.37	10.10	G7V	55 (5.5)	220	0.9075	1.100	0.908
CD-66 395	Octans	20.22	10.92	9.52	K0IV	190 (20)	250	0.2128	0.371	0.270
CD-72 248	Octans	20.42	10.91	9.24	K0IV	190 (20)	350:	0.235 576	0.236	0.236

the authors – Da Silva et al. 2013 – excludes CD-49 1902 from the Argus association.)

2 THE OBSERVATIONS

All measurements were made with the SAAO (South African Astronomical Observatory) STE4 CCD camera mounted on the SAAO 1.0-m telescope at Sutherland, South Africa. The field of view of the camera on the telescope is 5 × 5 arcmin^2. Pre-binning of the images was performed throughout, giving a reasonable readout time of about 17 s. Observations were cycled through various combinations of the *UBVR* filterset – see Table 2 for an observing log. (Note that the *R* filter is a Cousins system R_C – but the subscript is omitted for convenience). For each star, exposure times were tailored both to changing atmospheric conditions (seeing and cloud cover) and to the specific filter. Ranges were 1–15 s in *R*, 1.5–20 s in *V*, 10–90 s in *B* and 100–200 s in *U*. Very poor conditions sometimes made observing through the *U* filter impractical, while exceptionally good (subarcsecond) seeing made for poor *R*- and *V*-band photometry (since exposure times had to be very short to avoid saturation).

Photometric reductions were performed using an automated version of DOPHOT (Schechter, Mateo & Saha 1993). Generally magnitudes determined from point spread function (PSF) fitting were preferred over aperture photometry, since the noise levels were lower. The exception was CD-49 1902, for which aperture photometry proved superior. As a general rule, aperture photometry is more accurate for bright stars, and PSF photometry for fainter stars. In this particular case, the stars described in the paper are of similar brightness, hence it is not obvious why aperture photometry works best for CD-49 1902, while PSF photometry is less noisy for the other stars. Some of the factors which may play roles are seeing, sky background brightness, relative brightnesses of the local comparison stars, and amount of cloud cover.

The analysis reported below was performed on differential magnitudes of the stars, calculated with respect to bright local comparison stars in the field of view.

Particular care was taken with the estimation of nightly zero-points, so that photometry from different nights could be combined with confidence. The methodology described in Koen (2013),

Table 2. The observing log. Numbers of measurements taken through the different filters are in column 4. Column 5 shows the range of formal uncertainties in the run zero-points, across all filters. The last three columns contain the range of uncertainties in the estimated colour indices, over the entire run.

Starting time (HJD 2450000+)	Filters	Run length (h)	*N*	Zero-point S.E.s (mmag)	$\sigma(U-B)$ (mmag)	$\sigma(B-V)$ (mmag)	$\sigma(V-R)$ (mmag)
CD-36 3202							
6657.3032	*UBVR*	7.0	126–127	1.0–1.1	2.1–4.3	2.4–4.9	2.9–6.0
6658.2998	*UBVR*	6.9	114–117	1.0–1.1	2.0–4.4	2.3–4.5	2.6–5.3
6660.2852	*UBVR*	7.4	133–135	1.0–1.1			
6661.2891	*UBVR*	3.1	56–59	1.0–1.1	3.0–6.2	4.5–9.5	5.3–12.3
CD-49 1902							
5903.3237	*BVR*	2.6	71–74	2.2–3.2		1.6–3.1	1.9–4.0
5904.2983	*BVR*	7.1	128–129	2.0–3.1		0.9–2.0	0.9–1.8
5905.2744	*UBVR*	7.7	102–112	2.0–2.4		1.2–2.5	1.5–3.6
5909.2847	*BVR*	4.8	100–106	2.0–3.1		0.9–2.5	1.1–2.8
CD-66 395							
5941.3081	*UBVR*	4.9	73–77	1.9–2.8	2.4–5.4	3.2–6.6	3.6–7.7
5942.3657	*UBVR*	5.5	68–78	1.9–2.8	2.7–6.3	2.2–5.7	2.7–7.0
6654.2822	*UBVR*	7.3	144–146	2.2–2.6	1.8–3.7	2.3–4.9	2.9–6.4
6655.2886	*UBVR*	5.5	89–91	2.4–2.9	2.5–5.4	2.7–5.9	3.3–7.5
6656.2803	*UBVR*	7.5	153–159	1.9–2.4	1.7–3.4	2.2–4.5	2.9–6.3
CD-72 248							
5906.2974	*UBV*	7.0	75–79	1.9–2.1		3.4–7.0	3.4–7.3
5938.2988	*UBVR*	7.1	79–84	1.6–2.5	3.0–5.6	3.1–6.6	3.3–9.0
5940.2808	*UBVR*	6.8	64–69	1.7–2.9	2.6–6.1	3.7–10.0	4.5–10.9
6651.2891	*UBVR*	4.9	61–63	2.1–2.9	2.3–5.0	3.5–7.8	5.1–11.5
6652.3389	*UBVR*	4.8	67–72	2.0–2.8	2.8–5.5	3.1–6.4	3.7–9.0

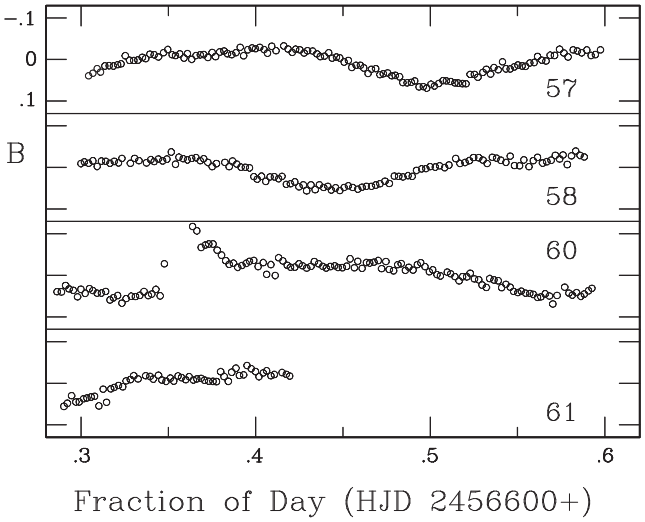

Figure 1. Light curves of CD-36 3202 in the *B* band. Panels are labelled with the last two digits of the Julian Day of observation. The light curve for HJD 2456660 is truncated, in order that detail of lower level variability remains clearly visible. See therefore also Fig. 2.

applicable when not all local standards are observed on all nights, was used. In essence, this is based on minimizing

$$\sum_j \sum_k (m_{jk} - \mu_j - \Delta_k)^2,$$

where m_{jk} is the magnitude of calibrating star (i.e. local comparison) k on night j; μ_j is the true photometric zero-point for night j; and Δ_k is the true mean magnitude of star k. Such standardization can be challenging, since in practice the set of calibrating stars may change from night to night. See also e.g. Reed & FitzGerald (1982), Manfroid & Heck (1983), Honeycutt (1992), Padmanabhan et al. (2008) and Regnault et al. (2009). Column 5 of Table 2 gives the range of zero-point uncertainties (across filters) for each observing run.

A collection of light curves is plotted in Figs 1–8 (Figs 6–8, which show *U* filter variability, are only available online as Supporting Information). Roughly sinusoidal variability and almost constant light levels are the most common forms seen – as expected for WTTS. The exception is the substantial flare in CD-36 3202, observed on HJD 2456660 (Fig. 2), which is discussed in detail in Section 5.

In keeping with many previous studies, it is found that amplitudes of variability increase with decreasing wavelength (e.g. Herbst et al. 1994). Generally the slopes of amplitude against wavelength are mild, suggesting dark spots on the stellar surfaces (Stahler & Palla 2004). Amplitudes can change dramatically over the course of a few days (Figs 3 and 5). This contrasts with satellite observations of four very young WTTS by Siwak et al. (2011), in which amplitudes changed little over the course of 2 or 3 weeks of continuous monitoring.

3 FOURIER ANALYSIS OF THE SAAO DATA

The primary tool used to study periodicities in variable stars is the Fourier spectrum. The periodogram, or power spectrum, is usually defined as

$$I(\omega) = \frac{1}{N}\left\{\left[\sum_t (y_t - \overline{y})\cos\omega t\right]^2 + \left[\sum_t (y_t - \overline{y})\sin\omega t\right]^2\right\},$$

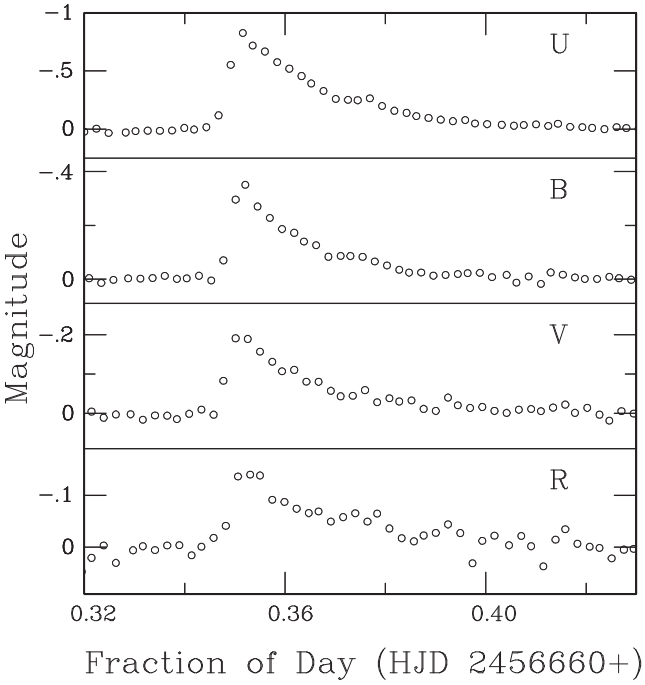

Figure 2. Detail of part of the light curves of CD-36 3202 obtained on HJD 2456660, showing a flare. The measurements have been pre-whitened by subtraction of the underlying periodic variability. Panels are labelled with filter names. Note the different scales on the vertical axes of the different panels.

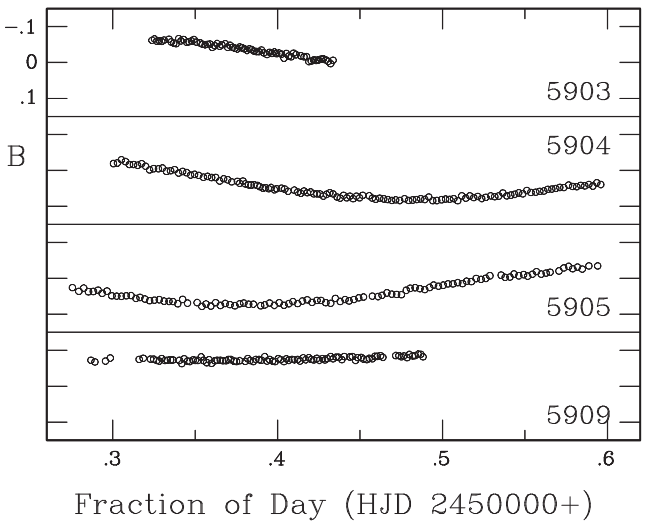

Figure 3. Light curves of CD-49 1902 in the *B* band. Panels are labelled with the last four digits of the Julian Day of observation.

where $\omega = 2\pi/P$ is the angular frequency corresponding to period P; y_t is the magnitude measured at time t; and $\overline{y}$ is the mean magnitude. The amplitude spectrum $S(\omega)$ is obtained from the transformation

$$S(\omega) = 2\sqrt{\frac{I(\omega)}{N}};$$

this has the advantage that peaks at signal frequencies have heights equal to signal amplitudes, i.e. direct physical interpretation of $S(\omega)$ is easier than $I(\omega)$.

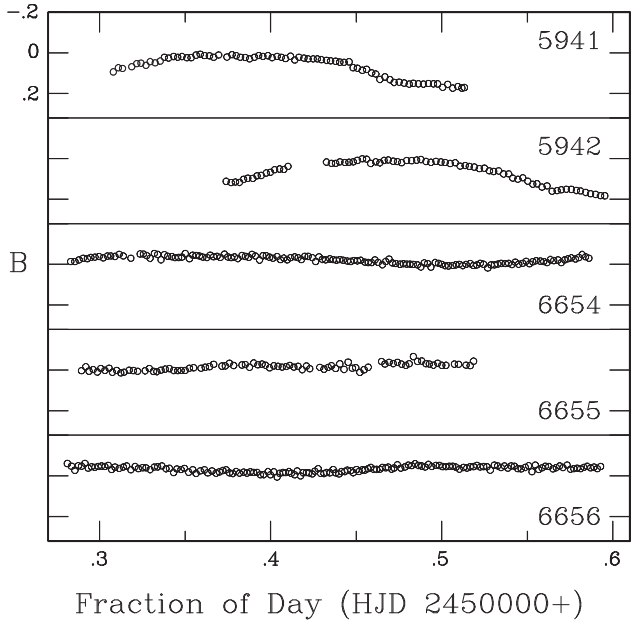

Figure 4. Light curves of CD-66 395 in the *B* band. Panels are labelled with the last four digits of the Julian Day of observation.

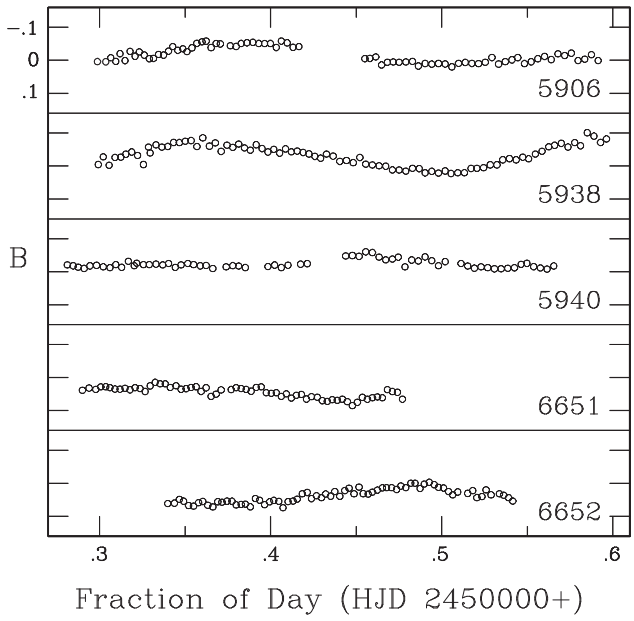

Figure 5. Light curves of CD-72 248 in the *B* band. Panels are labelled with the last four digits of the Julian Day of observation.

In this section, amplitude spectra of the photometry obtained at SAAO are investigated.

3.1 CD-36 3202

The flare during the third run on the star is clearly atypical compared to the data from the other three nights, and it is excluded in the consideration of periodicities: it is discussed at some length in Section 5. Fig. 1 favours the shorter (5.6 h) over the longer (7.4 h) of the two published periods in Table 1. (The corresponding frequencies are 4.25 and 3.26 d^{-1}.) The shorter period is confirmed by amplitude spectra of the data: frequencies at which the amplitude spectra show largest peaks are in the range 4.213–4.240 d^{-1} for the *UBVR* data. Furthermore, substantial peaks are also found at frequencies 7.44 (*U*), 8.48 (*B*, *V*) and 7.45 (*R*) d^{-1}; these are evidently the first harmonic, and its 1 d^{-1} alias.

The results of fitting the ASAS frequency 4.2494 d^{-1}, and its first harmonic, to the data are in Table 3. Remarkably, the amplitude of the first harmonic is virtually identical in all filters. A glance at Fig. 1 shows the probable origin of the harmonic term: a slight depression in the light curves near light maxima. The impression is that this is a geometric, rather than temperature, effect – i.e. that it may be due to obscuration of part of the stellar surface.

3.2 CD-49 1902

Inspection of Fig. 3 shows that amplitude of variability during the last night was much lower than during the preceding three runs, hence it is excluded from the analysis. Periodograms of the *BVR* data from the first three nights have maxima in the 2.246–2.247 d^{-1} range, but if the frequency of least-squares fit is made adjustable, those lie in the range 2.196–2.203 d^{-1}. The CD-49 1902 periods given in Table 1 correspond to frequencies of 1.1019 (ASAS) and 0.9091 (Messina et al. 2011) d^{-1}. Periods derived from the multicolour photometry are therefore half of the ASAS value. Examination of the fits to the SAAO data reveals that the first night's results are discrepant, with the observations extending well beyond the range covered by the fitted sinusoids. More reasonable looking fits, with slightly smaller residual variances, are obtained by using double the periods (frequencies 1.115–1.123 d^{-1}), which agree reasonably with the ASAS value. The well-defined light curve minima in Fig. 3 are clearly separated by about 0.9 d, which is at odds with the 1.1 d period of Messina et al. (2011).

The results of fitting $f = 1.1019$ d^{-1} to the *BVR* data from the first three nights are in Table 3.

3.3 CD-66 395

The two published periods quoted in Table 1 are 5.1 h (ASAS) and 8.9 h (Messina et al. 2011), corresponding to alias frequencies of 4.70 and 2.70 d^{-1}, respectively. Scrutiny of Fig. 4 supports the intermediate alias 3.70 d^{-1} (period 0.27 d or 6.5 h).

There is a gap of almost two years between the first two, and last three nights of observing of this star. There is also a clear difference in the levels of variability during the two epochs. The earlier and later data are therefore analysed separately.

Amplitude spectra of the longer data set give peak frequencies in the range 3.656–3.674 d^{-1}. Results for all four filters show low-frequency excesses, pointing to either imperfect standardization, or small changes ($\sim$ a few millimagnitudes) in the mean light levels from night to night. Fig. 9 shows the residual spectra, once the primary variations and the low-frequency features have been pre-whitened from the combined three nights of data. The most prominent feature in Fig. 9 is the 8 mmag peak at $f = 7.36$ d^{-1} in the *U* filter residuals. The second highest alias peak in the *B* data is at the very similar frequency (7.38 d^{-1}). The most obvious explanation for these peaks is that they are at first harmonics of the principal 3.67 d^{-1} frequencies in the data, pointing to non-sinusoidal variability.

Amplitude spectra of the shorter data set (consisting of the first two nights) are quite interesting. For all four filters prominent peaks (ranging from 50 mmag in *R* to 85 mmag in *U*) are seen, at frequencies in the range 4.57–4.59 d^{-1}, with strong (14–26 mmag) secondary peaks in the range 8.30–8.33 d^{-1}. It seems plausible

Table 3. The results of fitting sinusoids to the SAAO observations of the four target stars. Amplitudes are in millimagnitudes, phases in radians. Formal standard errors of estimated amplitudes and phases are given in brackets.

CD-36 3202		Frequency: $f = 4.2494$ d^{-1} + first harmonic		
	U	*B*	*V*	*R*
		Fundamental frequency		
Amplitude	42 (0.9)	38 (0.7)	33 (0.9)	28 (0.9)
Phase	−1.07 (0.021)	−0.96 (0.017)	−0.96 (0.025)	−0.97 (0.033)
		First harmonic frequency		
Amplitude	11 (0.7)	11 (0.9)	11 (0.8)	9 (0.9)
Phase	−1.69 (0.077)	−1.58 (0.055)	−1.49 (0.073)	−1.54 (0.10)
CD-49 1902		Frequency: $f = 1.1019$ d^{-1}		
		B	*V*	*R*
Amplitude		137 (1.3)	119 (1.1)	101 (1.1)
Phase		2.314 (0.0097)	2.330 (0.0095)	2.341 (0.011)
CD-66 395		Frequency: $f = 3.70$ d^{-1}		
	U	*B*	*V*	*R*
HJD 5941-5942				
Amplitude	98 (1.8)	82 (1.6)	71 (1.6)	57 (1.6)
Phase	0.51 (0.016)	0.52 (0.017)	0.53 (0.020)	0.56 (0.025)
HJD 6654-6656				
Amplitude	23 (0.8)	18 (0.9)	13 (0.8)	12 (1.0)
Phase	0.82 (0.036)	0.79 (0.050)	0.83 (0.059)	0.84 (0.082)
CD-72 248		Frequency: $f = 4.245$ d^{-1}		
	U	*B*	*V*	*R*
HJD 6651-6652				
Amplitude	26 (1.5)	21 (1.3)	20 (1.5)	18 (1.7)
Phase	0.78 (0.058)	1.11 (0.062)	1.13 (0.072)	1.01 (0.095)

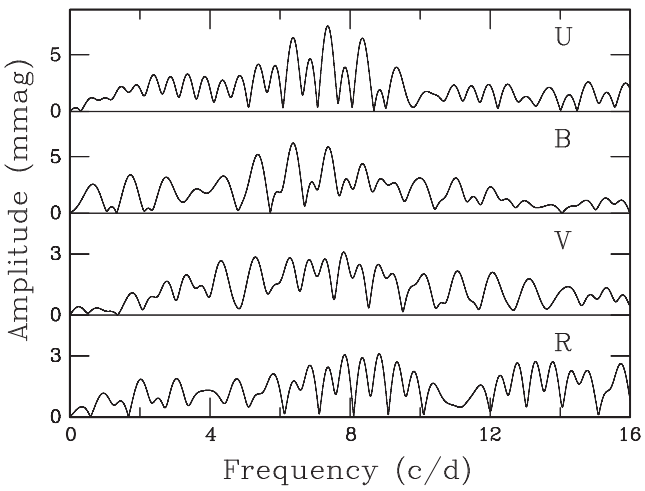

Figure 9. Amplitude spectra of the residuals, after pre-whitening of the most prominent frequencies from the combined last three runs on CD-66 395.

that the latter frequencies are 1 d^{-1} aliases of the first harmonics of 3.66 d^{-1} (see the preceding paragraph). It seems reasonable to assume that the ∼4.58 d^{-1} variations are aliases of 3.66 d^{-1}, but the difference between 3.58 and 3.66 is large in terms of the formal frequency standard errors.

It is cautiously concluded that the primary frequency of variability is 3.70 d^{-1}, and that its first harmonic may also be detectable if the amplitude at the primary frequency is larger than about 15 mmag. Table 3 contains amplitudes and phases of sinusoids fitted to the data with $f = 3.70$ d^{-1}.

3.4 CD-72 248

The frequency and amplitude of the single sinusoid which best fits the ASAS data are 4.24487 (2.0E−5) d^{-1} and 16 (1.9) mmag, where numbers in the brackets are standard errors. Further support for this 0.23 d (5.5 h) period, as listed also in Table 1, can be seen in the top two panels of Fig. 5.

It is instructive to compare panels two and three of Fig. 5, obtained 48 h apart. Fitting the ASAS frequency independently to the data from these two nights leads to the information in Table 4. Curiously, although the minimum light levels are similar during the two nights, the *relative* variability is much more pronounced in the blue on HJD 2455940, although the fit is not particularly good (Fig. 10). If variability is due to spots, then this would suggest a rapid change from a large coolspot to a small hotspot (e.g. Stahler & Palla 2004), although it is conventionally assumed that hotspots only occur on CTTSs (e.g. Petrov 2003). An alternative, probably more plausible, interpretation of the light curves from the second of these nights is that there is minimal variability aside from a hot low amplitude flare starting near HJD 2455940.44.

It is no surprise that data from the first two nights of observing do not phase together well. The last two nights, on the other hand, were consecutive, and amplitudes appear to be similar. Table 3 has the results of fitting a sinusoid with a frequency of 4.245 d^{-1} to these data. The shallow slope of amplitude versus wavelength is noteworthy.

4 COLOUR VARIATIONS AND SPOT PARAMETERS

The photometry can be used to deduce colour variations of the stars. This can be done in a variety of ways, one of which is illustrated here.

Table 4. A comparison of the amplitudes and phases of independent fits to two nights of CD-72 248 data. The frequency of the fitted sinusoid was assumed fixed at the value determined from the ASAS data, namely 4.245 d^{-1}.

	Amplitudes		Phases	
Filter	5938 (HJD 2450000+)	5940 (HJD 2450000+)	5938 (HJD 2450000+)	5940 (HJD 2450000+)
U	57 (1.9)	15 (2.2)	−0.53 (0.035)	0.30 (0.14)
B	44 (1.8)	12 (1.6)	−0.45 (0.041)	0.54 (0.14)
V	39 (1.4)	5 (2.5)	−0.51 (0.037)	− 0.49 (0.50)
R	36 (1.7)	6 (2.6)	−0.56 (0.046)	− 0.46 (0.47)

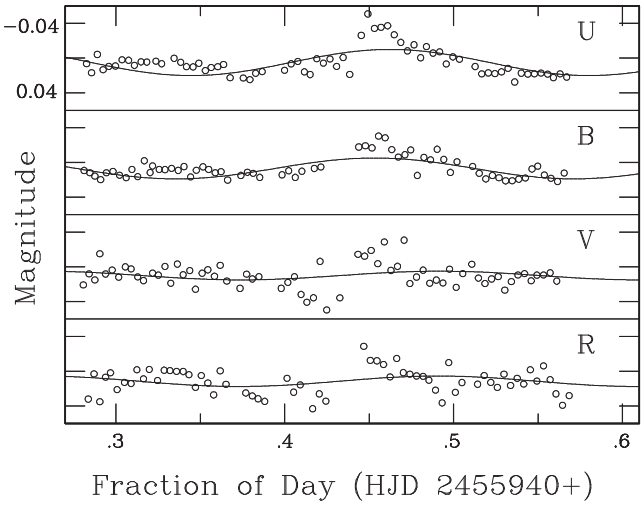

Figure 10. Sinusoids fitted to the third night's measurements of CD-72 248. The frequency was fixed at the value 4.244 87, as determined from ASAS observations of the star.

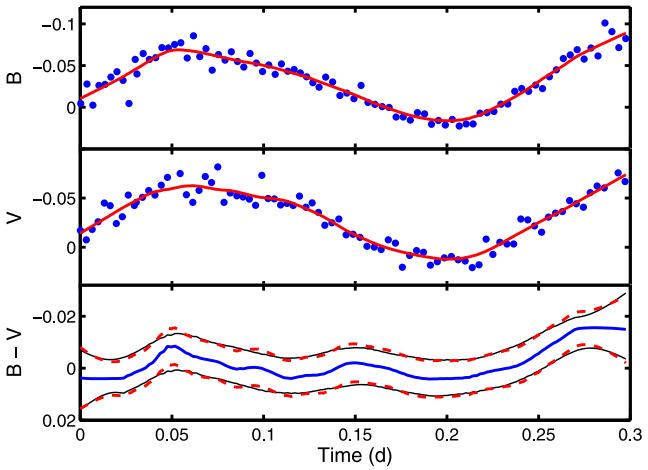

Figure 11. Observations of CD-72 248 in *B* (top panel) and *V* (middle panel), obtained during HJD 2455938. Dots represent measurements and the solid lines loess smooths. The estimated $(B - V)$ index is plotted in the bottom panel, together with 95 per cent (thin solid line) and ±2 standard deviations (thick broken lines) confidence intervals. Time is measured with respect to the start time of the run. Note the different scales on the vertical axes of the three panels.

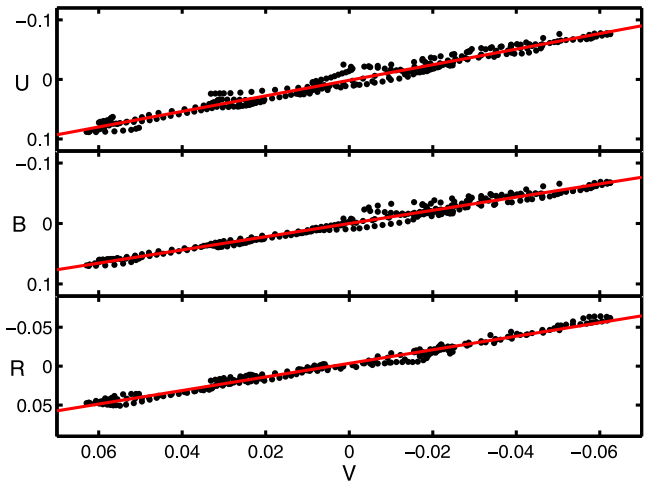

Figure 12. The relationship between the *UBR* magnitudes and *V* magnitude, for CD-72 248. The magnitude zero-points are arbitrary. Results for the other three stars are similar.

In order to estimate colour indices, the observed light curves were smoothed. This has the twin virtues of reducing noise, and of interpolation in time, so that measurements in the different filters can be estimated at common time points. The particular smoothing method used was 'loess' – see e.g. Cleveland & Devlin (1988), Cleveland, Devlin & Grosse (1988) or modern texts on data analysis. In the present context, the time interval spanned by the observations is covered by typically 120 equally spaced points. At each of these a weighted linear regression is performed over an interval covering 15–30 per cent of the run length. Interval lengths were chosen individually for each run: longer intervals give smoother results over the run, while shorter intervals preserve more detail.

An illustration, selected to be typical of most of the data, can be found in Fig. 11. Also shown is the estimated $(B - V)$ colour index, with confidence intervals. The confidence intervals were obtained by bootstrapping, using the residuals from the loess smooths – for a discussion of bootstrapping, see e.g. Efron & Tibshirani (1993). Two points about the confidence limits are worth noting: first, the 95 per cent and $\pm 2\sigma$ intervals are closely similar, which means σ values can reliably be used to obtain confidence intervals. Secondly, it is obvious that the confidence intervals are wider near the endpoints of the interval covered by the observations. Both maximum and minimum values of σ are therefore given in Table 2, for each estimated colour index.

A different way of representing the colour information is to study the interrelationship between the magnitudes measured in the different filters. This was done by again using loess regression on the *UBVR* data in order to interpolate to timepoints at which *V* magnitudes were measured. The first and last 7.5 per cent of the smoothed time series were discarded, since, as remarked above, the loess estimates are less accurate near the endpoints.

Results for CD-72 248 can be seen in Fig. 12: data for all the runs are included in the diagram. Clearly, the relationship between

Table 5. The results of regressing *UBR* magnitudes on *V* magnitudes, for each star. Standard errors of the estimated slopes are given in brackets. The number of data pairs is *N*; two figures are given for CD-49 1902 (no observations in *U*) and CD-72 248 (no *R* observations in the first run). The range covered by the *V* values is in column 3. The residual scatter σ (in mmag) in the regression fits is also given.

Star	*N*	ΔV	*U*		*B*		*R*	
			Slope	σ	Slope	σ	Slope	σ
CD-36 3202	260	0.077	1.24 (0.019)	6.7	1.14 (0.014)	5.1	0.86 (0.013)	4.6
CD-49 1902	0/358	0.147			1.087 (0.004)	4.1	0.867 (0.002)	2.1
CD-66 395	465	0.173	1.323 (0.008)	7.0	1.170 (0.005)	4.6	0.878 (0.006)	4.7
CD-72 248	310/246	0.125	1.31 (0.013)	7.8	1.09 (0.010)	5.7	0.873 (0.007)	4.1

magnitudes in the different filters is close to linear, with very modest residual scatter. The results of linearly regressing the *UBR* data on *V* are summarized in Table 5. The scatter in the top panel of Fig. 12 is the largest, at about 8 mmag. It is noteworthy that the slopes of the *R* versus *V* regression lines are, within the errors, identical for the four stars. There is also very little difference between the *B* on *V* regression slopes. In fact, the only difference of note between results for the different stars is the slope of the CD-36 3202 $U-V$ regression which is significantly shallower than the corresponding values for CD-66 395 and CD-72 248.

An explanation for the linear magnitude–magnitude relations is elaborated in Appendix A, in terms of variations in the coverage factor *f* of a dark spot on the stellar surface. It is shown that to good approximation

$$m(\lambda) = c_\lambda - 1.086 \ln F_2(T_2, \lambda) + 1.086 f \left[1 - \frac{F_1(T_1, \lambda)}{F_2(T_2, \lambda)}\right], \quad (1)$$

where F_1 and F_2 are the fluxes, at wavelength λ, of the star-spot and undisturbed stellar photosphere, which are at respective temperatures T_1 and T_2. The zero-point of the magnitude m_λ is determined by the constant c_λ. Equation (1) implies that, as *f* varies, a linear relation is traced between the magnitudes measured through different filters. The slope of this relation depends only on T_1 and T_2, so that if the photospheric temperature T_2 is known, the spot temperature T_1 is the only unknown parameter. Contemporaneous measurements of brightness through two filters is therefore sufficient to deduce the star-spot temperature – though a sufficient range of variation should be covered so that the slope of the magnitude–magnitude relation (A6) can be accurately determined. Of course, if observations are made through more filters, there is an overdetermined set of equations, and T_1 can be estimated more accurately.

The model presented in Appendix A can also be used to estimate the range Δf of the star-spot filling factor. Results are given in Table 6, both for simple blackbody fluxes and for *UBVRI* fluxes calculated from model atmosphere spectra (e.g. Buser & Kurucz 1992). The particular model tabulations used in this paper were in the ubvp00k2odfnew.dat and coubesp00k2odfnew.dat files downloaded from http://kurucz.harvard.edu/grids/gridp00odfnew. There is little difference between the numerical values calculated assuming $\log g = 3.5$ and those following from $\log g = 4.0$. Spot temperatures predicted by the blackbody radiation model are generally somewhat higher than those calculated from the Kurucz models; the same goes for Δf. The predicted slopes are in reasonable agreement with the observed values in Table 5.

The differences between the photospheric temperature T_2 and the spot temperature T_1 is $\Delta T = T_2 - T_1 \sim 800$–$900$ K for all the stars except CD-49 1902, for which $\Delta T \sim 1150$ K. This may be related to the facts that this star is rather hotter, and also rotates more slowly than the other three objects. Filling factor ranges for CD-49 1902 and CD-72 248 are quite similar (estimates in the range 16–19 per cent). Values of Δf are larger for CD-66 395 (23–28 per cent), and smaller for CD-36 3202 (10–11 per cent). Both temperatures and filling factors of all four stars lie comfortably

Table 6. The results of fitting the model of Appendix A to the slopes and *V* magnitude ranges, in Table 5. The temperatures of the spotted and unspotted surfaces of the star are T_1 and T_2. Values of T_2 were obtained from the tabulation of pre-main-sequence star temperatures on spectral type by Pecaut & Mamajek (2013). Calculations were done with blackbody spectra ('BB' in column 3) and with atmospheric model spectra, assuming two different values of $\log g$. The range of filling factors is Δf. The rest of the table gives predicted straight line regression slopes, for comparison with the observed values in Table 5.

Star	T_2	$\log g$	T_1	Δf	Slope			
					U	*B*	*R*	*I*
CD-36 3202	5040	BB	4250	0.11	1.253	1.128	0.893	0.794
		3.5	4240	0.10	1.257	1.114	0.892	0.773
		4.0	4270	0.10	1.256	1.113	0.887	0.759
CD-49 1902	5530	BB	4390	0.18	1.211	1.110	0.904	0.814
		3.5	4340	0.17	1.216	1.107	0.906	0.811
		4.0	4370	0.17	1.221	1.106	0.900	0.802
CD-66 395	5280	BB	4610	0.28	1.327	1.159	0.876	0.767
		3.5	4450	0.23	1.331	1.149	0.880	0.777
		4.0	4470	0.23	1.331	1.144	0.874	0.765
CD-72 248	5280	BB	4520	0.19	1.291	1.144	0.884	0.781
		3.5	4400	0.16	1.295	1.135	0.887	0.785
		4.0	4430	0.16	1.296	1.131	0.881	0.773

within the ranges observed for T Tauri stars (e.g. Bouvier & Bertout 1989, and the review by Petrov 2003).

5 THE FLARE IN CD-36 3202

It has been remarked in the literature (e.g. Herbst et al. 1994; Stahler & Palla 2004) that, on short time-scales, WTTS light curves in *U* are more erratic than those at longer wavelengths. This is ascribed to flaring activity. Comparison of Figs 6–8 (online only) with Figs 1, 3–5 show very little evidence for this contention. In fact, in the more than 100 h of monitoring reported here, Fig. 2 is the only clearcut observation of any flaring behaviour.

The flare light curve is best studied by first removing the background variability. As was seen in Section 3.1, three runs on CD-36 3202 produced light curves which can be well represented by a sinusoid plus its first harmonic. The fit to those flare-free data was used to predict the variability during HJD 2456660, when the flare was observed; if the predicted variability is subtracted from the observations the light curves in Fig. 2 are obtained.

Two features of the flares are worth remarking on. First, there is a 'standstill' in the interval 0.37–0.38 on the descending branch of the light curves, particularly evident in *U* and *B*. This phenomenon has been ascribed to the simultaneous operation of two different cooling mechanisms – radiation and conduction (Mullan 1977). If correct, this could place limits on the physical conditions at the flare site. Secondly, the maxima appear to be more extended at longer wavelengths, persisting in *V* and *R* after the onset of declines in *U* and *B*.

The time resolution of the observations plotted in Fig. 2 was about 3.4 min (203 s). The flare rise time can therefore be seen to be about 10 min. The full duration of the flare was roughly 0.08 d, or 1.9 h. Amplitudes were approximately 0.83, 0.35, 0.19 and 0.14 mag in *UBVR*. If the flare is treated as an additional source of radiation, then at its peak the colour indices were $(U-B)=-0.48$, $(B-V)=-0.16$ and $(V-R)=-0.05$. These numbers resemble those of main-sequence B6-B7 stars – respective indices for such stars are $(U-B)=-0.50$, $(B-V)=-0.14$, $(V-R)=-0.06$; and $(U-B)=-0.46$, $(B-V)=-0.13$ and $(V-R)=-0.06$ (Pecaut & Mamajek 2013). The effective temperatures of such stars are 14 500 and 14 000 K. Alternatively, a least-squares fit to a blackbody spectrum of the three flux ratios $F(U)/F(V)=1.80$, $F(B)/F(V)=1.16$ and $F(R)/F(V)=0.96$, gives a best value of 8900 K. The fit to a blackbody is rather poor though: the drop from *U* to *B* at this temperature is not steep enough, and the drop from *V* to *R* too steep.

There was a predicted light curve minimum at HJD 2456660.327, and the flare started 0.02 d (about 30 min) later. Given that the period is 5.6 h (see below), this result is consistent with the finding in Fernández et al. (2004) who observed that large flares in the WTTS V410 Tau occurred near phases of minimum.

A crude estimate of the energy released in the flare can made, with improvement pending, amongst other quantities, absolute (i.e. zero-point calibrated) measurements of *U* and *R*. Torres et al. (2006) measured $V=11.22$ and $B=11.84$. Using $(U-B)=0.60$ and $(V-R)=0.49$ for a K2V star (Pecaut & Mamajek 2013), $U\approx 12.44$ and $R\approx 10.73$. Absolute magnitudes $M_U=6.8$, $M_B=6.2$, $M_V=5.6$ and $M_R=5.1$ then follow from the distance of 135 pc given by Torres et al. (2008). The formula

$$L_\lambda = 10^{-0.4(M_\lambda - 4.75)}\,\mathrm{L}_\odot\ ,$$

where L_λ is the luminosity of the star measured in filter λ, M_λ is the corresponding absolute magnitude and $\mathrm{L}_\odot = 3.8\times10^{33}$ erg s^{-1} is the solar (bolometric) luminosity, then gives quiescent luminosities L_q of roughly 0.15, 0.26, 0.46 and 0.72 times solar in *UBVR*, respectively.

Denoting the instantaneous flare luminosity by L_f,

$$(L_q+L_\mathrm{f})/L_q = 10^{-0.4(m_{q+f}-m_q)} = 10^{-0.4\Delta m_\mathrm{f}}$$

and

$$L_\mathrm{f} = L_q\left(10^{-0.4\Delta m_\mathrm{f}}-1\right)\ .$$

The total energy release is then

$$E=\int L_\mathrm{f}\,\mathrm{d}t = L_q\int\left(10^{-0.4\Delta m_\mathrm{f}}-1\right)\,\mathrm{d}t. \qquad (2)$$

Integration of the four flare profiles in Fig. 2 requires smoothing of the light curves. This task can be simplified considerably if a suitable mathematical form can be fitted to the flares. A variety of functions were tried, amongst them

$$f(t)=A\exp-\left[\frac{\tau_1}{t-t_s}+\frac{t-t_s}{\tau_2}\right]$$

(Norris et al. 2005) which is widely used to model gamma-ray bursts. The most convincing fits were obtained using the alternative four-parameter model

$$f(t) = A\psi^{\xi+1}(t)\exp[-\psi(t)]$$
$$\psi(t)=\left[1+\xi\left(\frac{t-\mu}{\sigma}\right)\right]^{-1/\xi} \qquad \xi>0,\ t\geq\mu-\sigma/\xi. \qquad (3)$$

If $A=1/\sigma$ the function equals the generalized extreme value probability density function (PDF; e.g. Kotz & Nadarajah 2000), which is useful since the integral over the PDF is unity, and hence

$$\int f(t)\,\mathrm{d}t = A\sigma.$$

Since fitting the form (3) to the flare provides estimates of *A* and σ, the integral does not need to be evaluated explicitly.

The numerical values of the integrals in (2) are 1892, 573, 365 and 302 s (*UBVR*, respectively), and the corresponding flare energies are 11, 5.9, 6.6 and 8.6×10^{35} erg. These values can be compared to flares observed in the WTTS V410 Tau by Fernández et al. (2004): energy ranges were $1.4–4.2\times10^{35}$ (*U*), $0.4–3\times10^{35}$ (*B*) and $0.2–2.4\times10^{35}$ (*V*) erg. The distance assumed for V410 Tau was 136 pc (i.e. essentially the same as for CD-36 3202) and the spectral type is similar to that of CD-36 3202; the flare amplitudes and durations seen in the present case are therefore somewhat larger.

6 THE ASAS PHOTOMETRY

The ASAS photometry analysed here was obtained during the years 2000–2009, in an approximate *V* band. For CD-66 395 about 40 per cent of the time intervals between measurements were less than a day; for the other three stars the most common interval was around two days. Fewer than 10 per cent of intervals between observations were longer than 10 d, with occasional very long seasonal gaps.

Reduced data for five different aperture sizes are available, with error estimates for each individual measurement. The aperture with the smallest mean error was selected: for all three stars the latter figure was below 0.035 mag. Outlying measurements were removed, and low-order polynomials fitted to the data, and subtracted, to correct for very long term drifts in mean brightnesses. The final number of data ranged from 570 for CD-72 248 to 1180 for CD-66 395.

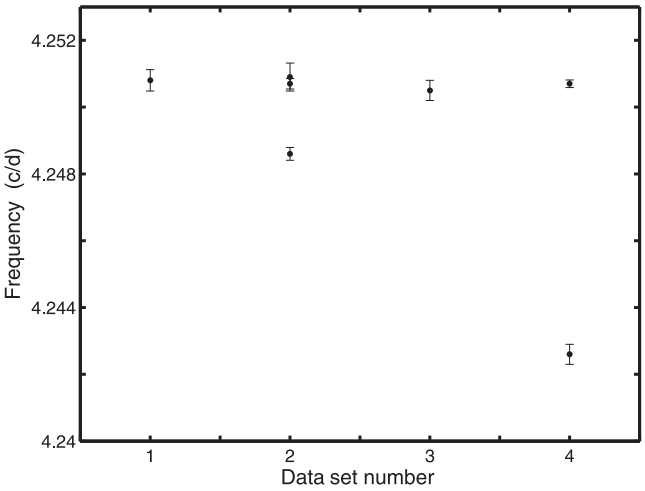

Figure 13. The frequencies of prominent sinusoidal variations in the ASAS observations of CD-36 3202. The timebase of the measurements was split into four blocks, with gaps of at least 100 d between blocks. The frequency interval scrutinised was 4.15–4.35 d^{-1}. Error bars are $\pm 2\sigma$, where σ is the formal uncertainty of the least-squares fit to the sinusoid.

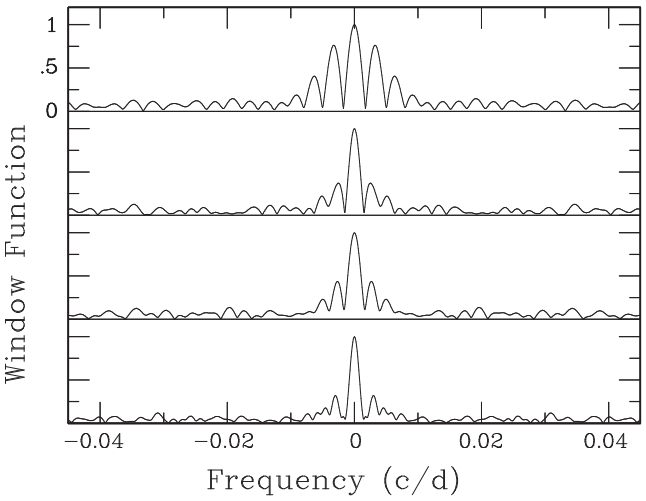

Figure 17. Window functions of a subdivision of the CD-72 248 ASAS data into four consecutive intervals separated by at least 100 d. The time spans covered by the four intervals were 390, 666, 526 and 780 d, respectively. There is, of course, also substantial aliasing at intervals of 1 d^{-1} (i.e. outside the frequency range plotted).

The frequency content of non-overlapping sections of the ASAS light curves are now studied. Each set of observations, spanning about 8.5 years, has typically four gaps longer than 100 d and these were used to subdivide the data. The partitioning of the data resembles the procedure used by Messina et al. (2010), but the time intervals used here are considerably longer (390–829 d, as opposed to two months). Each of the data sections was again individually detrended by low-order polynomials. Amplitude spectra were then calculated over narrow intervals (0.2–0.3 d^{-1}) centred on the frequencies determined in Section 3 of this paper. The central 0.1 d^{-1} or so of the interval was examined for significant features – 'significant' as compared to the noise levels defined by spectra over the rest of the frequency interval.

The detailed investigation of the frequency content of the data subsets is based on successive pre-whitening: the frequency of peak power is used as starting point in a search for the sinusoid which fits the data with maximal amplitude. This sinusoid is then subtracted from the data, and the process repeated to find the next best-fitting sine function. The iteration is continued until it is subjectively decided that only noise remains in the data.

The results can be seen in Figs 13–16 (Figs 14–16 are only available online as Supporting Information). Because of the long time baseline of each data set the formal standard errors on the frequencies are quite small (typically of the order of 10^{-4} d^{-1}), and hence the ± 2 standard errors indicated in the plots are often of similar sizes as the plotting symbols. It should be borne in mind that these errors definitely underestimate the true uncertainties: for example, results would be affected if low frequencies were pre-whitened differently.

The following points can be made.

(1) Fig. 17 shows the window functions of the four sections of CD 72-248 data. The window functions of the other three partitioned data sets look quite similar. The sidelobes of the central peaks are due to one and two cycle per year aliases. Note that, the first data section aside, these are quite small.

(2) The expectation is that star-spot configurations would change over the durations of data sets this long. This should manifest in the frequency domain as a number of closely spaced peaks in the periodograms of the data. This is not quite what is seen in Figs 13–16: the frequency spacings are much larger than might have been expected.

(3) Generally, there is more than one periodicity in a data section. Exceptions can be seen in the CD-36 3202 and CD-72 248 data (Figs 13 and 16). Consider, for example, the first two sets of observations of CD-72 248. These two single-frequency data sets, respectively, consist of 115 measurements over 390 d, and 154 measurements over 666 d. These numbers are comparable to those for the third data set – 125 observations, spread over 526 d, and also very similar to most of the data sets for other stars. The paucity of frequencies can therefore not be ascribed to the data span and/or number of measurements. It appears that this star, and CD-36 3202, may have sustained intervals during which spot configurations are stable or simple.

(4) The substantial difference between the two frequencies found in data sets 1 and 2 of CD-72 248 (Fig. 16) is puzzling. The error bars clearly show that the difference is not due to a lack of frequency resolution. Another possibility is that these are aliases, but the window functions (Fig. 17) demonstrate that this is probably not the case.

(5) It is furthermore noteworthy that within the errors, both frequencies referred to in point 4 also seem to be present in data sets 3 and 4. One possibility is that spots are formed at two different latitude regions, and that differential rotation of the stellar surface is responsible for the distinct frequencies.

(6) There are single frequencies which are persistent in the CD-36 3202 and CD-66 395 data sets. In the case of CD-49 1902 two frequencies ($\sim$1.116 and $\sim$1.102 d^{-1}) are present throughout.

There is a fairly strong case for the presence of multiple periodicities in some of the stars. The most obvious explanation is that star-spots are present at different latitudes at different times, and that the stars rotate at different rates at different latitudes. Results are summarized in Table 7, which may be compared with the study by Barnes et al. (2005) of differential rotation in 10 late-type stars. The data in Table 5 lie within the range of values in Barnes et al. (2005) – see particularly their fig. 3. Siwak et al. (2011) deduced equator to pole rotation frequency differences in the range zero

Table 7. Probable differential rotation extracted from the ASAS photometry of the four stars. The third column gives the spread in the frequencies extracted from the observations. Frequencies have been converted to angular frequencies $\Omega = 2\pi f$, and log-transformed, in the last two columns, to facilitate comparison with Barnes et al. (2005).

Star	Frequency f (d^{-1})	Frequency range Δf (d^{-1})	$\log_{10}\Omega$ (log rad d^{-1})	$\log_{10}\Delta\Omega$ (log rad d^{-1})
CD-36 3202	4.24	0.0082	1.43	−1.29
CD-49 1902	1.10	0.014	0.84	−1.06
CD-66 395	3.70	0.016	1.37	−1.00
CD-72 248	4.25	0.0061	1.43	−1.42

to 0.007 d^{-1} from their observations of four young WTTSs, i.e. generally somewhat smaller than for the subjects of this paper.

7 CONCLUDING REMARKS

(1) For three of the stars the original ASAS periods are confirmed (Table 1). In the case of CD-66 395, both published periods are incorrect. The accurately determined periods can be used to gain some information about inclination angles of rotation axes:

$$\sin i = \frac{8.64 \times 10^4 P(v \sin i)}{2\pi \times 6.96 \times 10^5 R} = \frac{0.020 P v \sin i}{R},$$

where P is the period (in d), R the stellar radius in solar units, and $v \sin i$ is in km s^{-1}. Results are that $R \sin i = 0.79$, 0.99, 1.01 and 0.88 for CD-36 3202, CD-49 1902, CD-66 395 and CD-72 248, respectively. It follows that the radii of CD-49 1902 and CD-66 395 are probably somewhat larger than solar.

The ages of the associations to which the stars belong are in the range 20–40 Myr. At an age of 30 Myr the radius of a 0.6 (1.0) $M_\odot$ star is about 0.72 (1.01) $R_\odot$ (Stahler & Palla 2004). The numbers in the preceding paragraph suggest that these theoretical radii may be underestimates, or that CD-49 1902 and CD-66 395 may be somewhat younger than 30 Myr. In any case, the inclination to the line of sight of the rotation axes of these two stars should be quite close to 90°.

(2) The only flare was seen in observations of the only star with an emission line spectrum (CD-36 3202 – see Table 1). The generalized extreme value PDF (equation 3) was shown to be a useful model for the flare; fitting this form to the flare immediately provides the flare energy.

(3) The observations reported here were used to show that magnitude changes in the different filters are linearly related. The slopes of the various linear relations are generally very similar for the four stars. The model described in the appendix could be used to deduce spot temperatures, and the range of filling factors (Table 6).

(4) An implication of the material in the Appendix is that the temperatures of coolspots can be estimated from relatively small photometric data sets: the only requirement is that a wide enough magnitude baseline be covered that the slopes of the linear magnitude–magnitude relations can be accurately determined.

(5) The results presented in Section 6 suggest that there may be a wealth of information regarding differential rotation in spotted stars, to be gleaned from surveys such as ASAS. Numerical results for the four stars of this paper are presented in Table 7.

ACKNOWLEDGEMENTS

The author is grateful to those maintaining the Simbad data base in Strasbourg, France, and to SAAO for allocating telescope time. Abundant use was made of the 2MASS, *GALEX* and *WISE* catalogues. This research was supported by a grant from the South African National Research Foundation. Comments from the referee led to improvements in the paper.

REFERENCES

Barnes J. R., Collier Cameron A., Donati J.-F., James D. J., Marsden S. C., Petit P., 2005, MNRAS, 357, L1
Bianchi L., Herald J., Efremova B., Girardi L., Zabot A., Marigo P., Conti A., Shiao B., 2011, Ap&SS, 335, 161
Bouvier J., Bertout C., 1989, A&A, 211, 99
Buser R., Kurucz R. L., 1992, A&A, 264, 557
Cleveland W. S., Devlin S. J., 1988, J. Am. Stat. Assoc., 83, 596
Cleveland W. S., Devlin S. J., Grosse E., 1988, J. Econometrics, 37, 87
Da Silva L., Torres C. A. O., De La Reza R., Quast G. R., Melo C. H. F., Sterzik M., 2009, A&A, 508, 833
Da Silva L., D'Orazi V., Melo C., Torres C. A. O., Gieles M., Quast G. R., Sterzik M., 2013, MNRAS, 431, 1005
Efron B., Tibshirani R. J., 1993, An Introduction to the Bootstrap. Chapman & Hall, London
Fernández M. et al., 2004, A&A, 427, 263
Grankin K. N., Melnikov S. Yu., Bouvier J., Herbst W., Shevchenko V. S., 2007, A&A, 461, 183
Grankin K. N., Bouvier J., Herbst W., Melnikov S. Yu., 2008, A&A, 479, 827
Günther H. M. et al., 2010, A&A, 518, 54
Herbst W., Herbst D. K., Grossman E. J., Weinstein D., 1994, AJ, 108, 1906
Herbst W., Eislöffel J., Mundt R., Scholz A., 2007, in Reipurth B., Jewitt D., Keil K., eds, Protostars and Planets V. Univ. Arizona Press, Tucson, p. 297
Honeycutt R. K., 1992, PASP, 104, 435
Kiraga M., 2012, Acta Astron., 62, 67
Koen C., 2011, MNRAS, 411, 813
Koen C., 2012, MNRAS, 419, 706
Koen C., 2013, MNRAS, 431, 1048
Kotz S., Nadarajah S., 2000, Extreme Value Distributions. Theory and Applications. Imperial College Press, London
Manfroid J., Heck A., 1983, A&A, 120, 302
Messina S., Desidera S., Turatto M., Lanzafame A. C., Guinan E. F., 2010, A&A, 520, A15
Messina S., Desidera S., Lanzafame A. C., Turatto M., Guinan E. F., 2011, A&A, 532, A10
Mullan D. J., 1977, ApJ, 212, 171
Norris J. P., Bonnell J. T., Kazanas D., Scargle J. D., Hakkila J., Giblin T. W., 2005, ApJ, 627, 324
Padmanabhan N. et al., 2008, ApJ, 674, 1217
Pecaut M. J., Mamajek E. E., 2013, ApJS, 208, 9
Petrov P. P., 2003, Astrophysics, 46, 506
Pollacco D. et al., 2006, PASP, 118, 848
Reed B. C., FitzGerald M. P., 1982, A&A, 111, 81
Regnault N. et al., 2009, A&A, 506, 999

Schechter P. L., Mateo M., Saha A., 1993, PASP, 105, 1342
Silva-Valio A., Lanza A. F., 2011, A&A, 529, 36
Siwak M., Rucinski S. M., Matthews J. M., Kuschnig R., Guenther D. B., Moffat A. F. J., Sasselov D., Weiss W. W., 2011, MNRAS, 415, 1119
Skrutskie M. F. et al., 2006, AJ, 131, 1163
Smith K. W., Jones D. H. P., Clarke C. J., 1996, MNRAS, 282, 167
Stahler S. W., Palla F., 2004, The Formation of Stars. Wiley-VCH, Weinheim
Torres C. A. O., Quast G. R., Da Silva L., De La Reza R., Melo C. H. F., Sterzik M., 2006, A&A, 460, 695
Torres C. A. O., Quast G. R., Melo C. H. F., Sterzik M., 2008, in Reipurth B., ed., ASP Monograph Publications, Handbook of Star Forming Regions, Volume II. The Southern Sky. Astron. Soc. Pac., San Francisco, p. 757

APPENDIX A: THE LINEAR MAGNITUDE–MAGNITUDE RELATIONS

The following simple model is adopted (Stahler & Palla 2004): star-spots occupy a fraction f of the visible stellar surface. The flux at wavelength λ from the spotted region of the star is $F_1(\lambda)$. The unspotted surface radiates flux $F_2(\lambda)$. The observed magnitude at wavelength λ is then

$$\begin{aligned} m(\lambda) &= c_\lambda - 2.5\log_{10}[fF_1(\lambda) + (1-f)F_2(\lambda)] \\ &= c_\lambda - 1.086\ln F_2(\lambda) - 1.086\ln\{1 + f[F_1(\lambda)/F_2(\lambda) - 1]\}, \end{aligned} \tag{A1}$$

where c_λ is a constant which depends on the wavelength, but not on the filling factor f or either flux.

For fixed λ, F_1 and F_2, the Taylor series expansion of (A1) with respect to $\delta = f[F_1(\lambda)/F_2(\lambda) - 1]$ is then

$$\begin{aligned} m(\lambda) &= c_\lambda - 1.086\ln F_2(\lambda) - 1.086\sum_{k=1}^{\infty}(-1)^{k-1}\delta^k/k \\ &= c_\lambda - 1.086\ln F_2(\lambda) + 1.086\sum_{k=1}^{\infty}\left[1 - \frac{F_1(\lambda)}{F_2(\lambda)}\right]^k f^k/k. \end{aligned} \tag{A2}$$

The convergence of the sum in (A2) will evidently be rapid: since $F_1/F_2 < 1$ for dark star-spots,

$$\left[1 - \frac{F_1(\lambda)}{F_2(\lambda)}\right]^k < 1, \qquad f^k < 1, \qquad 1/k \le 1$$

and hence the product of the three factors will be small.

To make the results more concrete, assume blackbody radiation

$$F_j(\lambda) \equiv B_\lambda(T_j) = \beta_\lambda\left[\exp\left(\frac{\alpha}{\lambda T_j}\right) - 1\right]^{-1} \qquad j = 1, 2, \tag{A3}$$

where β_λ and α are constants, with $\alpha = 1.44 \times 10^8$ if the wavelength is measured in Å and temperature in K. Since $\exp(\alpha/\lambda T) \gg 1$,

$$B_\lambda(T_1)/B_\lambda(T_2) \approx \exp\left(\frac{\alpha}{\lambda T_2} - \frac{\alpha}{\lambda T_1}\right)$$

and it follows that

$$m(\lambda) \approx c'_\lambda + 1.086\left\{\frac{\alpha}{\lambda T_2} + \sum_{k=1}^{\infty}\left[1 - \exp\left(\frac{\alpha}{\lambda T_2} - \frac{\alpha}{\lambda T_1}\right)\right]^k f^k/k\right\}. \tag{A4}$$

Where $c'_\lambda = c_\lambda - 1.086\log\beta_\lambda$. The linear approximation

$$m(\lambda) \approx c'_\lambda + 1.086\left\{\frac{\alpha}{\lambda T_2} + \left[1 - \exp\left(\frac{\alpha}{\lambda T_2} - \frac{\alpha}{\lambda T_1}\right)\right] f\right\} \tag{A5}$$

is demonstrated in Fig. A1, for *UBVR* effective wavelengths, with $T_2 = 5200$ and $T_1 = 4500$ K. The approximation is evidently excellent at filling factors less than about 40 per cent. There are substantial deviations from linearity at the shorter wavelengths for larger filling factors. The quadratic approximation

$$\begin{aligned} m(\lambda) \approx c'_\lambda + 1.086\Bigg\{&\frac{\alpha}{\lambda T_2} + \left[1 - \exp\left(\frac{\alpha}{\lambda T_2} - \frac{\alpha}{\lambda T_1}\right)\right] f \\ &+ \frac{1}{2}\left[1 - \exp\left(\frac{\alpha}{\lambda T_2} - \frac{\alpha}{\lambda T_1}\right)\right]^2 f^2\Bigg\} \end{aligned}$$

is denoted by the plus signs in the figure.

Equation (A5) implies that

$$\begin{aligned} m(\lambda_j) \approx c(\lambda_0, \lambda_j, T_1, T_2) &+ \left[1 - \exp\left(\frac{\alpha}{\lambda_j T_2} - \frac{\alpha}{\lambda_j T_1}\right)\right] \\ &\times \left[1 - \exp\left(\frac{\alpha}{\lambda_0 T_2} - \frac{\alpha}{\lambda_0 T_1}\right)\right]^{-1} m(\lambda_0), \end{aligned} \tag{A6}$$

where $c(\lambda_0, \lambda_j, T_1, T_2)$ is a zero-point and λ_0 is a reference wavelength. This is illustrated in Fig. A2, together with the exact results calculated from equations (A1) and (A3), with f ranging zero to unity. It is clear that at the bright end (large fluxes, small filling factors) the linear equation is adequate. In particular (at least for the assumed temperatures), linearity is a good assumption for amplitudes $\Delta V \lesssim 0.2$ mag (e.g. the observations described in this paper).

A striking aspect of Fig. A2 is that the linear approximation magnitudes do not cover the full range induced by the filling factor variations. The origin of this deficiency is visible in Fig. A1, at large values of f. A consequence is that the range of filling factors Δf cannot be simply estimated from equation (A5) as

$$\Delta f = 0.92\Delta m\left[1 - \exp\left(\frac{\alpha}{\lambda T_2} - \frac{\alpha}{\lambda T_1}\right)\right]^{-1}.$$

Instead, the exact form

$$\Delta f = [\exp(0.92\Delta m) - 1]/\left[\frac{F_2}{F_1} - 1\right]$$

could be used.

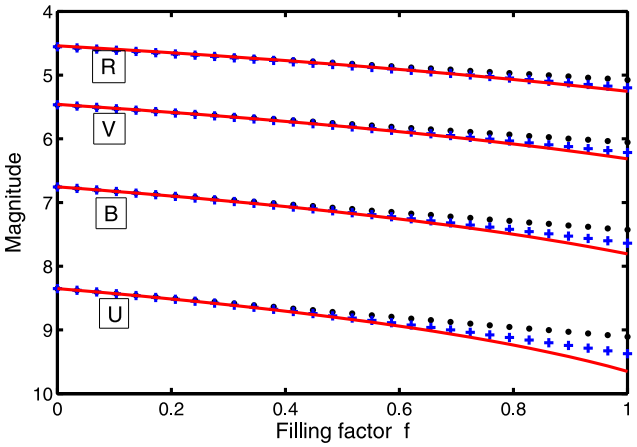

Figure A1. Magnitudes as a function of filling factors, for fixed spot and stellar surface temperatures ($T_1 = 4500$ and $T_2 = 5200$, respectively). Solid lines, dots and plus signs, respectively, denote the exact results (equation A1), the linear approximation (equation A5), and the quadratic approximation obtained by truncating the series in equation (A4) after the second-order term. Magnitude zero-points in the figure are arbitrary.

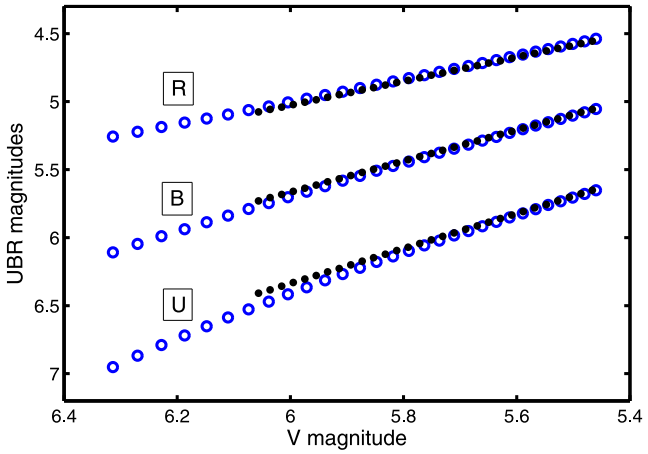

Figure A2. *UBR* magnitudes plotted against corresponding *V* magnitudes, for fixed spot and stellar surface temperatures ($T_1 = 4500$ and $T_2 = 5200$, respectively). Magnitude zero-points are arbitrary. Open symbols show exact values calculated from (A1) and (A3), while the dots represent the linear approximation (A6). Each plotted point corresponds to a particular value of the filling factor, from $f = 0$ at $V = 5.46$ to $f = 1$ at $V = 6.31$.

In order to obtain estimates of the spot temperature T_1 and the range Δf of the filling factor the observed magnitude–magnitude slopes are compared to those predicted by equation (A1). The following recipe is followed.

(i) First obtain a value of T_2, from the spectral type of the star (using, for example, table 5 of Pecaut & Mamajek 2013). Also choose a reference filter.

(ii) Assume values of Δf and T_1.

(iii) Select a grid of filling factor values $0 \leq f \leq \Delta f$, and calculate corresponding magnitudes from equations (A1) and (A3), for each filter.

(iv) Using the results from (iii), regress the other magnitudes on the reference magnitude to obtain predicted line slopes.

(v) Calculate the sum of squares

$$\mathrm{SS} = \sum [\text{Observed slope} - \text{Predicted slope}]^2$$

or, more conveniently,

$$\mathrm{SS} = [(\text{Observed range of reference magnitude}) - (\text{Predicted range of reference magnitude})]^2 + \sum [\text{Observed slope} - \text{Predicted slope}]^2.$$

(vi) Iterate over steps (ii)–(v) to find values of T_1 and Δf which minimize SS.

SUPPORTING INFORMATION

Additional Supporting Information may be found in the online version of this article:

Figure 6. Light curves of CD-36 3202 in the *U* band. Panels are labelled with the last two digits of the Julian Day of observation. The light curve for HJD 2456660 is truncated, in order that detail of lower level variability remains clearly visible. See therefore also Fig. 2.

Figure 7. Light curves of CD-66 395 in the *U* band. Panels are labelled with the last four digits of the Julian Day of observation.

Figure 8. Light curves of CD-72 248 in the *U* band. Panels are labelled with the last four digits of the Julian Day of observation.

Figure 14. As for Fig. 13, but showing results for CD-49 1902. The frequency interval covered was 1.05–1.15 d^{-1}.

Figure 15. As for Fig. 13, but showing results for CD-66 395. The frequency interval covered was 3.55–3.85 d^{-1}. Note that the time spacing of the measurements of this star gave rise to three well-separated blocks of observations, rather than four.

Figure 16. As for Fig. 13, but showing results for CD-72-248. The frequency interval covered was 4.15–4.35 d^{-1}. (http://mnras.oxfordjournals.org/lookup/suppl/doi:10.1093/mnras/stv316/-/DC1).

Please note: Oxford University Press are not responsible for the content or functionality of any supporting materials supplied by the authors. Any queries (other than missing material) should be directed to the corresponding author for the article.

This paper has been typeset from a TEX/LATEX file prepared by the author.